Research Article | Vol. 26, No. 8 | 16 Apr 2018 | OPTICS EXPRESS 9502
Optics EXPRESS

Highly efficient all-optical beam modulation utilizing thermo-optic effects

VLADIMIR LIBERMAN,* PAUL D. ROBINSON, GEOFFREY P. GEURTSEN, SHANE M. TYSK AND MICHAEL W. GEIS

Lincoln Laboratory, Massachusetts Institute of Technology, Lexington, Massachusetts 02421, USA
**vlad@ll.mit.edu*

Abstract: Suspensions of plasmonic nanoparticles can diffract optical beams due to the combination of thermal lensing and self-phase modulation. Here, we demonstrate extremely efficient optical continuous wave (CW) beam switching across the visible range in optimized suspensions of 5-nm Au and Ag nanoparticles in non-polar solvents, such as hexane and decane. On-axis modulation of greater than 30 dB is achieved at incident beam intensities as low as 100 W/cm^2 with response times under 200 μs, at initial solution transparency above 70%. No evidence of laser-induced degradation is observed for the highest intensities used. Numerical modeling of experimental data reveals thermo-optic coefficients of up to -1.3×10^{-3} /K, which, to our knowledge, is the highest observed to date in such nanoparticle suspensions.

OCIS codes: (240.6680) Surface plasmons; (350.6830) Thermal lensing; (140.3360) Laser safety and eye protection.

References and links

1. J. Shen, R. D. Lowe, and R. D. Snook, "A model for cw laser induced mode-mismatched dual-beam thermal lens spectrometry," Chem. Phys. **165**(2-3), 385–396 (1992).
2. K. L. Jansen and J. M. Harris, "Double-beam thermal lens spectrometry," Anal. Chem. **57**(13), 2434–2436 (1985).
3. Y. E. Geints, N. S. Panamarev, and A. A. Zemlyanov, "Transient behavior of far-field diffraction patterns of a Gaussian laser beam due to the thermo-optical effect in metal nanocolloids," J. Opt. **13**(5), 055707 (2011).
4. B. Palpant, M. Rashidi-Huyeh, G. Gallas, S. Chenot, and S. Fisson, "Highly dispersive thermo-optical properties of gold nanoparticles," Appl. Phys. Lett. **90**(22), 223105 (2007).
5. M. Rashidi Huyeh, M. Shirdel Havar, and B. Palpant, "Thermo-optical properties of embedded silver nanoparticles," J. Appl. Phys. **112**(10), 103101 (2012).
6. H. Aleali, L. Sarkhosh, M. Eslamifar, R. Karimzadeh, and N. Mansour, "Thermo-optical properties of colloids enhanced by gold nanoparticles," Jpn. J. Appl. Phys. **49**(8), 085002 (2010).
7. R. Karimzadeh and N. Mansour, "The effect of concentration on the thermo-optical properties of colloidal silver nanoparticles," Opt. Laser Technol. **42**(5), 783–789 (2010).
8. L. Sarkhosh, H. Aleali, R. Karimzadeh, and N. Mansour, "Large thermally induced nonlinear refraction of gold nanoparticles stabilized by cyclohexanone," Phys. Status Solidi., A Appl. Mater. Sci. **207**(10), 2303–2310 (2010).
9. M. Sheik-Bahae, A. A. Said, and E. W. Van Stryland, "High-sensitivity, single-beam n($_2$) measurements," Opt. Lett. **14**(17), 955–957 (1989).
10. M. Mashayekh and D. Dorranian, "Size-dependent nonlinear optical properties and thermal lens in silver nanoparticles," Optik (Stuttg.) **125**(19), 5612–5617 (2014).
11. K. Moutzouris, M. Papamichael, S. C. Betsis, I. Stavrakas, G. Hloupis, and D. Triantis, "Refractive, dispersive and thermo-optic properties of twelve organic solvents in the visible and near-infrared," Appl. Phys. B **116**(3), 617–622 (2014).
12. L. Deng, K. He, T. Zhou, and C. Li, "Formation and evolution of far-field diffraction patterns of divergent and convergent Gaussian beams passing through self-focusing and self-defocusing media," J. Opt. A, Pure Appl. Opt. **7**(8), 409–415 (2005).
13. M. Zhengle, Q. Lingling, H. Fei, L. Yang, W. Chen, and C. Ya, "Thermal-induced nonlinear optical characteristics of ethanol solution doped with silver nanoparticles," Chin. Opt. Lett. **7**(10), 949–952 (2009).
14. V. Pilla, G. G. G. Costa, and T. Catunda, "Applications of Fresnel-Kirchhoff diffraction integral in linear and nonlinear optics: a didactic introduction," Proc. SPIE **4419**, 728–731 (2001).
15. V. Pilla, E. Munin, and M. R. R. Gesualdi, "Measurement of the thermo-optic coefficient in liquids by laser-induced conical diffraction and thermal lens techniques," J. Opt. A, Pure Appl. Opt. **11**(10), 105201 (2009).

#318128 https://doi.org/10.1364/OE.26.009502
Journal © 2018 Received 12 Jan 2018; revised 25 Mar 2018; accepted 27 Mar 2018; published 3 Apr 2018

Optics EXPRESS

16. S. E. Bialkowski, "Photothermal spectroscopy methods for chemical analysis," in *Chemical Analysis: A Series of Monographs on Analytical Chemistry and Its Applications,* J. D. Winefordner, ed., (John Wiley & Sons, Inc., 1996), Vol. 134.
17. G. A. López-Muñoz, J. A. Pescador-Rojas, J. Ortega-Lopez, J. S. Salazar, and J. A. Balderas-López, "Thermal diffusivity measurement of spherical gold nanofluids of different sizes/concentrations," Nanoscale Res. Lett. **7**(1), 423 (2012).
18. P. Laven, "MiePlot: a computer program for scattering of light from a sphere using Mie theory & the Debye series, *http://www.philiplaven.com/mieplot.htm*, 2017.
19. D. D. Evanoff and G. Chumanov, "Size-Controlled Synthesis of Nanoparticles. 2. Measurement of Extinction, Scattering, and Absorption Cross Sections," J. Phys. Chem. B **108**(37), 13957–13962 (2004).
20. J. M. Zook, V. Rastogi, R. I. Maccuspie, A. M. Keene, and J. Fagan, "Measuring Agglomerate Size Distribution and Dependence of Localized Surface Plasmon Resonance Absorbance on Gold Nanoparticle Agglomerate Size Using Analytical Ultracentrifugation," ACS Nano **5**(10), 8070–8079 (2011).
21. A. J. Hallock, P. L. Redmond, and L. E. Brus, "Optical forces between metallic particles," Proc. Natl. Acad. Sci. U.S.A. **102**(5), 1280–1284 (2005).
22. S. Fardad, A. Salandrino, M. Heinrich, P. Zhang, Z. Chen, and D. N. Christodoulides, "Plasmonic Resonant Solitons in Metallic Nanosuspensions," Nano Lett. **14**(5), 2498–2504 (2014).
23. J. Jung and T. G. Pedersen, "Polarizability of supported metal nanoparticles: Mehler-Fock approach," J. Appl. Phys. **112**(6), 064312 (2012).
24. M. C. Frare, R. Signorini, V. Weber, and R. Bozio, "Gold nanoparticles as optical limiting materials against CW lasers," Proc. SPIE **8901**, 890113 (2013).

1. Introduction

Laser-induced thermo-optic beam modulation occurs when an incident beam is absorbed in a medium, producing local heating around the beam axis. The local heating, in turn, results in a temperature-dependent refractive index distribution, producing both a thermal lens effect and diffraction of the original beam. Any absorbing medium will, in principle, cause this effect, which can serve as a sensitive diagnostic of impurities in an otherwise-transparent solvent [1, 2]. As we show below, the effect is maximized in liquid suspensions with low thermal conductivity and high thermo-optic coefficient.

Dispersions of nanoparticles (NPs), such as Au and Ag, have received attention as a thermal-lens medium because of their good stability, strong absorption due to localized plasmonic effects and potential synergy of the thermo-optic properties between the solvent medium and the colloidal material itself [3–8]. Typically, thermo-optic nonlinearities in such colloidal system are studied utilizing the so-called "closed aperture Z-scan" method [9], where a cuvette with colloidal nanosuspension is translated through focus and the far-field nonlinear refraction of the transmitted beam is measured as a function of intensity. Such measurements include both intensity-dependent Kerr effect as well as thermo-optic nonlinearities. Aleali et al. [6] used this method to characterize thermo-optic response of 15-nm diameter Au NPs in water. For the highest colloid concentrations of 20 ppm, they recorded $dn/dT = -0.31 \times 10^{-4}$/K at 532 nm. Karimzadeh and Mansur [7] have measured thermo-optic coefficient of aqueous dispersions of Ag NPs. For the highest volume fraction of 8.7 ppm, they observe $dn/dT = -0.92 \times 10^{-4}$/K at 532 nm. Mashayekh and Dorranian [10] studied thermo-optic effects of Ag NPs dispersed in acetone. While their studies suggest large thermal lens effects, the derived thermo-optic coefficients vary by an order of magnitude, depending upon the method used. Finally, Sarkhosh et al. [8] have studied Au NP suspensions in cyclohexanone at 532 nm. For 1 ppm volume fraction, they observe a doubling of the thermo-optic coefficient due to the presence of Au NPs, though their measured overall dn/dT of -1.49×10^{-4}/K is not particularly high, compared to that of organic solvents [11].

In an alternative experimental approach, Geints et al. [3] have applied the traditional thermal lens attenuation techniques to study time-dependent beam attenuation in plasmonic suspensions as a potential application for CW laser blocking [12, 13]. Their measurements explicitly demonstrated the importance of large thermo-optic coefficient with decreased suspension thermal conductivity. However, response times no faster than seconds were demonstrated in that study with no attempt to optimize the laser blocking.

Optics EXPRESS

In this work, we demonstrate efficient all-optical broadband CW laser switching in Ag and Au nanocolloidal suspensions with microsecond time response and on-center beam blocking exceeding three orders of magnitude of the incident beam intensity. Efficient thermo-optic switching for incident intensities as low as 100 W/cm^2 has been demonstrated. No laser-induced damage or de-stabilization of suspension has been observed under all the experimental conditions, with laser intensities exceeding 1500 W/cm^2. Initial suspension transparency exceeded 70% over the full visible wavelength range. This performance was achieved by optimization of solvent and nanoparticle (NP) properties.

The remainder of this manuscript is structured in three parts. First, we present diffraction theory that will be used to model experimental data and allow us to extract thermo-optic coefficients. Next, we present our experimental arrangement and discuss results of the all-optical laser beam manipulation. Finally, we discuss system implications for efficient laser beam blocking, including a proposed system configuration, as well as time-response and critical power onset for practical implementations.

2. Theory

We assume that the incident laser beam is partially absorbed in a suspension, leading to an axially symmetric temperature rise around the beam axis. We also assume that the absorption coefficient is temperature-independent, which is a safe assumption for low temperature rises predicted for this study. Due to the thermo-optic effect, the radial temperature rise induces a spatial variation in the refractive index, leading to a phase shift of the propagating beam that depends on the transverse distance from the beam's axis. The phase shift leads to two main effects: A) thermal lensing of the beam, whose behavior depends on the relative distance of the sample with respect to the incident beam waist and B) conical diffraction in the far field due to self-phase modulation [14, 15]. For experimental manifestation of these phenomena, see Fig. 3. Below, we will derive the expected far field beam profile, using the Fresnel–Kirchhoff diffraction formalism. All the terms used in our derivation are defined in Table 1.

Table 1. Definition of Terms Used in Equations throughout the Manuscript

Term	Definition
r	Radial distance in the far field
r_1	Radial distance at the cell entrance
t	Time
P_0	Incident power
E_0	Incident electric field magnitude
α	Absorption coefficient
f_a	Fraction of incident power absorbed
κ	Thermal conductivity
ω	Beam waist
L	Cell length
λ	Incident wavelength
T	Temperature
n	Refractive index
D	Thermal diffusivity
z_1	Distance between the cell and the waist of the beam
z_0	Rayleigh range of the beam
θ_{max}	Divergence angle of the outer diffraction ring

For an incident beam with Gaussian intensity, the temperature rise along the radial direction as a function of time can be expressed as [3]:

$$\Delta T(r,t) = \frac{P_0 \alpha}{4\pi\kappa}\left[\mathrm{E}_i\left(-\frac{r^2}{\omega^2}\right) - \mathrm{E}_i\left(-\frac{r^2}{\omega^2\left(1+4Dt/\omega^2\right)}\right)\right] \quad (1)$$

Optics EXPRESS

In the above, E_i is the exponential integral and the rest of the terms are defined in Table 1. Equation (1) assumes boundary conditions of ambient temperature at an infinite distance r and, thus, is strictly valid only for shorter times when the heat has not diffused to the walls of the cell, containing NP suspension. For the case of our beam diameters of <100 μm, cuvette width of 3 mm and thermal diffusivity of hexane of $8\text{x}10^{-6}$ m^2/sec [16], the equation is strictly valid for t << 1 sec, well within the time scales for transient behavior described in section 3. While our medium involves suspensions of nanoparticles in hexane, we assume that the thermal properties of the suspension are those of pure solvent for ppm-level concentrations of nanoparticles [17].

The induced temperature rise, described by Eq. (1), leads to a time-dependent phase shift of the incident Gaussian beam, given as

$$\Delta\varphi(r,t) = \frac{2\pi}{\lambda} L \frac{dn}{dT}(\lambda)\Delta T(r,t) \tag{2}$$

In the above equation, we explicitly highlight the wavelength dependence of the thermo-optic coefficient. As the incident Gaussian beam undergoes the phase shift, its far-field intensity at a distance d is given as a function of radial distance r and time t as [14, 15]:

$$I(r,t) = \left| \frac{i2\pi}{\lambda d} \exp\left[\frac{i2\pi}{\lambda d}\left(d + \frac{r^2}{2d} \right) \right] \int_0^\infty \exp\left(\frac{i\pi r_1^2}{\lambda d} \right) E_0 \exp\left(\frac{-r_1^2}{\omega^2} \right) \exp(-i\Delta\varphi) J_0\left(\frac{2\pi r r_1}{\lambda d} \right) r_1 dr_1 \right|^2 \tag{3}$$

In the above equation, J_0 is the zero-order cylindrical Bessel function. Equations (1 - 3) were used for modeling the experimental results presented in Section 3. For the on-axis transient experiments, we restricted r in Eq. (3) to the range, subtended by the on-axis detector, and performed averaging of intensity over that radial range as a function of time. Equations (1-3) were used to fit the experimental data assuming intensity-independent thermal parameters. Because of the different excitation wavelengths, we are specifically able to extract wavelength dispersion of the thermo-optic coefficient, dn/dT, from the experimental data. Other than the thermo-optic coefficient, all parameters were fixed either by experimental geometry or by solvent thermal properties, obtained from the literature, as indicated below.

Additionally, for understanding parametric dependence of the beam-blocking phenomenon, a useful approximation for on-axis time dependent intensity at small phase shifts, normalized to the initial intensity, is [1]:

$$\frac{I(t)}{I(0)} = \left[1 - \frac{P_0\left(1-e^{-\alpha L}\right)}{2\lambda\kappa} \frac{dn}{dT} \tan^{-1}\left(\frac{2V}{\omega^2 / 8Dt\left[9+V^2\right]+3+V^2} \right) \right]^2 \tag{4}$$

In Eq. (4), $V = z_1/z_0$, where z_1 is the distance between the cuvette and the waist of the beam, while z_0 is the Rayleigh range of the beam. Equation (4) can be used to understand decay-time dependence of on-axis intensity. For cell position close to beam waist, $V << 1$, and the inverse tangent function can be Taylor-expanded to show that characteristic decay time is inversely proportional to the thermo-optic coefficient and the incident laser power. Experimental results shown in section 3 bear out this dependence.

Finally, beam divergence due to the thermo-optic phenomenon can be estimated from the divergence angle of the outer diffraction ring [3]:

$$\theta_{\max} \sim \frac{0.3P_0\left(1-e^{-\alpha L}\right)}{\pi\omega\kappa} \left| \frac{dn}{dT} \right| \tag{5}$$

Optics EXPRESS

From Eq. (5), maximizing thermo-optic coefficient and incident power, while reducing thermal conductivity, will increase the thermal lensing effect. Additionally, beam divergence is not proportional to laser intensity, which would imply inverse proportionality to the square of beam size, but, rather, inversely proportional to the single power of beam size. We will discuss these implications in the section 4 of the manuscript.

3. Experimental description and results

3.1 Experimental setup

The experimental setup for time-dependent studies and diffracted beam profiling is shown in Fig. 1(a) and 1(b), respectively.

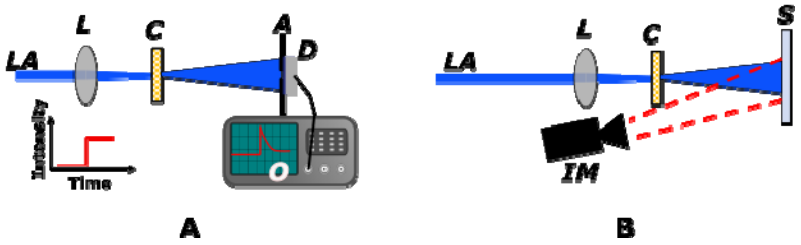

Fig. 1. A. Time-dependent measurement of beam blocking. Representative temporal shape of the incident beam is shown in the inset. B. Beam profiling of the incident laser beam in the far field. LA = Laser beam, L = lens, C = cuvette, A = aperture, D = detector, O = oscilloscope, S = screen, IM = imaging camera.

The light source for these experiments was provided by a three-laser spatial beam combiner (Oxxius, L4C), which included 405-nm, 633-nm and 785-nm sources. Each CW laser source included an integrated acousto-optic modulator (AOM) for shuttering individual beams with <2-ns time response. Because of additional turning mirrors (not shown in the figure), maximum available laser power on the sample was 5 mW for the 405-nm and 80 mW for the 633/785 nm lasers. All the incident power measurements were performed with a calibrated power meter (PM2, Coherent Corporation).

All the laser beams were focused onto a sample cuvette with a 150-mm focusing lens. The spot size in the center of the cuvette was 60 μm for the 405-nm beam and 90 μm for the 633/785 nm beams. The laser spot size was measured by placing an imaging camera (Wincam D from DataRay, Inc.) at the cuvette position. The cuvette length was 3 mm. After passing through the cuvette, the laser beam was incident on an apertured silicon photodiode positioned 26 cm way from the cuvette for the time-dependent experiments (Fig. 1(a)). The size of the aperture was 0.8 mm, and the rise time for the photodiode was ~1 ns. The signal was then fed to a 5 GHz oscilloscope for further processing.

For the screen visualization experiments, the laser beam exiting the cuvette was incident on a white screen 26-cm away from the cuvette. The resulting image on the screen was visualized with an imaging camera, Fig. 1(b). Here, both a high-resolution camera (Edmund Optics, E0-5012C, 2 megapixels, 60 frames per second) as well as a high-speed camera (Photron FASTCAM Mini AX200, 40 kilopixels, 500 frames per second) were used.

3.2 Nanoparticle suspensions

5-nm size Au and Ag NP dried powders (Nanocomposix, Inc.) were used as a starting material. For dispersion in non-polar solvents (hexane and decane), NPs were obtained with dodecanethiol capping agents, whereas for the aqueous suspensions, NPs were obtained with polyvinylpyrrolidone capping agents. Nanopowders were added into the appropriate solvent and sonicated for up to 30 minutes for full dispersion. The concentration of NPs in the solvent was adjusted so that transmission through the 3-mm pathlength was 70% (referenced to air) at the plasmonic resonance wavelength.

Optics EXPRESS

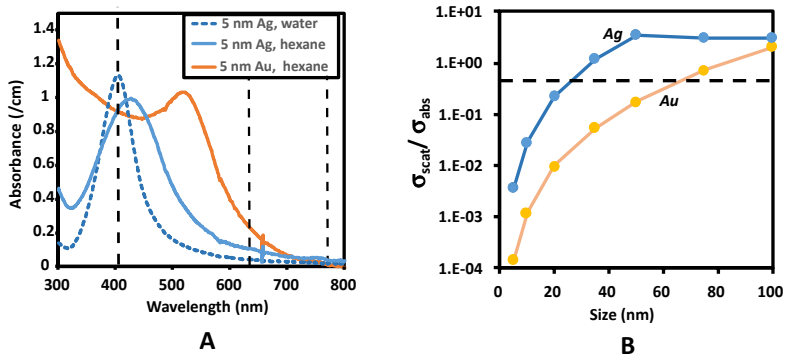

Fig. 2. A. Experimental spectral absorbance per cm of NP suspensions tested. Dashed vertical lines indicate wavelength positions of the incident lasers used. B. Computed ratio of scattering over absorption cross-sections of Ag and Au nanoparticles in hexane as a function of particle size at respective resonances.

Figure 2(a) shows measured absorbance per cm for the three nanocolloidal suspensions used in the experiments. In order to understand the relative scatter contribution as compared to the absorption, we computed the ratio of scattering cross-section over absorption cross-section for Au and Ag NPs in hexane, as a function of particle size, Fig. 1(b), with a MiePlot scattering code [18]. The cross-section ratio was computed at the respective resonance wavelength, which is near 400 nm for Ag and 530 nm for Au NPs. For our application of thermo-optic beam blocking, scattering is undesirable because it reduces clarity of the original suspension and reduces coupling efficiency of the incident beam with the suspension. We observe that for our small nanoparticle sizes of 5 nm, scattering contribution is negligible. However, for larger nanoparticle sizes, scattering contribution rises rapidly and exceeds absorption for 40-nm Ag particles and 80-nm Au particles, respectively. The rapid increase of scattering cross-section with size is due to the localized plasmonic resonance present in Au and Ag [19]. For larger nanoparticles, the cross-section at plasmonic resonance can exceed geometric cross-section by more than a factor of five.

Additionally, using MiePlot scattering code, based on spectral signatures from Fig. 2(a), we derived expected concentration, interparticle spacing and volume fraction for the Au and Ag NPs in hexane (see Table 2). Since Ag NPs have a stronger plasmonic cross-section, their concentration is significantly less than that of Au NPs. No interparticle interaction is expected for well-dispersed suspensions as the interparticle spacing greatly exceeds the particle diameter.

Table 2. Nanoparticle concentration, interparticle spacing and volume fraction, derived from computed per-particle cross-sections and experimental data presented in Fig. 2(a).

Suspension	Particle concentration (/cm^3)	Interparticle Spacing (μm)	Volume Fraction
5 nm Au NP/hexane	1.61×10^{13}	0.4	1×10^{-6}
5 nm Ag NP/hexane	8.5×10^{11}	1.1	5.6×10^{-8}

3.3 Beam imaging experiments

To demonstrate the phenomenology of thermo-optic effect, we continuously translated a cuvette containing 5-nm Au nanoparticles along incident beam focus, while irradiating it with a 633-nm laser and acquiring images with a high-speed camera on the far-field screen (as in Fig. 1(b)). Figure 3 shows three representative frames, obtained with the cuvette: (A) 2 cm in front of beam focus, (B) close to focus and (C) 2 cm behind focus. By using the high-speed camera, we are able to minimize any effects of convective flow, thus obtaining sharper images of diffractive fringes. The images clearly reveal dual phenomenology of thermal lensing and self-phase modulation. Because the thermo-optic coefficient of the colloidal

Optics EXPRESS

suspension is negative, the thermal lens formed by the suspension focuses the beam when placed in front of the original beam waist, Fig. 3(a), and diverges the beam when placed behind the beam waist, Fig. 3(c) [1]. When cuvette is placed close to focus, the thermal lensing effect is minimized. However, in all cases, diffraction fringes are observed, revealing self-phase modulation.

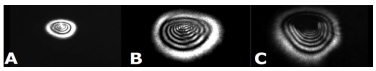

Fig. 3. 633-nm beam imaged in the far field by a high-speed camera, after it passes through a cuvette containing 5-nm nanoparticle suspension. A. The cuvette is placed 2 cm in front of focus. B. The cuvette is placed near focus. C. The cuvette is placed 2 cm past focus.

In the remaining experiments, the cuvette was placed within a mm past focus for ease of alignment and the far-field image on the screen was obtained with a high-resolution camera in the steady state, while varying the incident laser power. Figure 4 shows a series of such images obtained from a suspension of Au 5-nm NPs in hexane, irradiated with a 405-nm laser. Figure 4(a)-(d) shows experimental data, while Fig. 4(e)-(h) shows corresponding simulations obtained with Fresnel-Kirchoff diffraction integral, from Eq. (3). The thermo-optic coefficient used for these simulations, is derived from numerical fitting of the time-dependent data below, Figs. 7 and 8. The intensity of simulation data is normalized within each frame to the highest value. The beam spot is 60 μm at the waist inside the cuvette and the incident power across each row is 0.3, 1.7, 2.9 and 5.0 mW, respectively. The dashed red circles in the top row represent the region that contains 86% of the total beam power. For completeness, in Fig. 5 we show a radial temperature profile inside the cuvette that is used to compute the data of Fig. 4 (h). Equation (1) is used for this temperature simulation for a laser incident power of 5 mW at three time snapshots after the laser is turned on: 0.01 sec, 0.1 sec and 1 sec. The experimental images of Fig. 4 are acquired approximately one second after laser turn-on.

In general, good qualitative agreement is obtained between experiments and the simulations for both beam diameter and profile. This agreement presents another validation of the unusually high observed value of the thermo-optic coefficient, as derived more accurately from the time-dependent experiments in section 3.4. The experimental data do reveal more contrast in the on-axis beam rejection than simulations. The asymmetry in the experimental profiles may be due to convective effects, which are not taken into account in the simulation.

Images, similar to those shown in Fig. 4, were acquired for Au and Ag 5-nm NP suspensions for 405-nm, 633-nm and 785-nm wavelengths over a range of incident laser power. For all the above experiments, the beam spot grew with increased power, developing a hollow interior with one or more diffraction rings forming, similar to those shown in Fig. 3. Comparing integrated intensity for the images with increase in laser power shows no decrease in total energy, but, rather, a re-distribution of intensity into the diffraction rings. For each image, we have extracted the 86%-energy beam diameter, converted it to divergence angle and displayed the data as a function of incident power density (see Fig. 6). The lines passing through the symbols in the figure are linear fits, according to diffraction theory of Eq. (5). For 405-nm and 785 nm incident wavelengths, the divergence data are similar for both Au and Ag 5-nm NPs in hexane. The high slope for the 405-nm data arises from the large absorbance at this wavelength (see Fig. 2(a)). For the 633-nm beam, the Au NPs display higher divergence than Ag. The difference can be attributed to a combination of higher absorption of the Au suspension at this wavelength as well as higher effective thermo-optic coefficient.

Optics EXPRESS

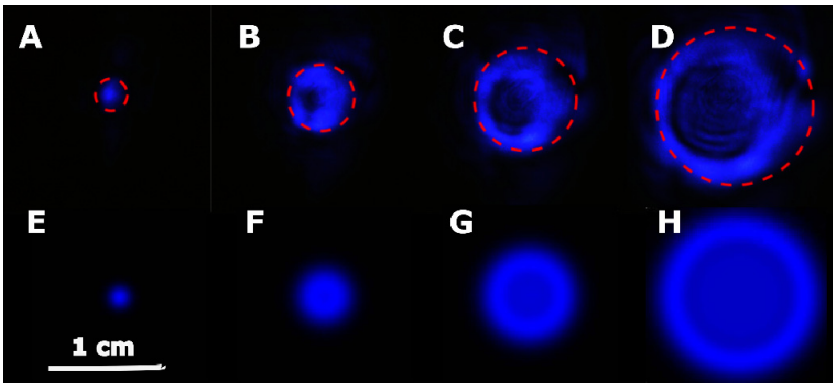

Fig. 4. Far-field beam profiles for 5-nm Au NP suspension in hexane, irradiated with a 405-nm laser.A-D are experimental measurements, while E-H are diffraction simulations from Eq. (3) (see text for details). The beam waist inside the cuvette is 60 μm and the beam power, from left to right, across each row is 0.3, 1.7, 2.9 and 5.0 mW, respectively.

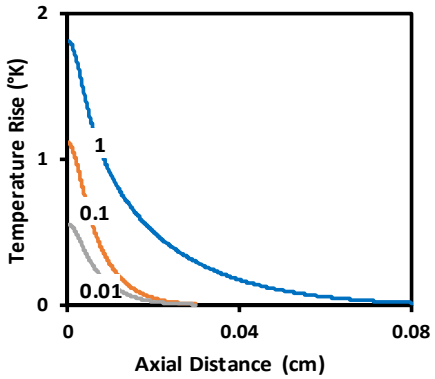

Fig. 5. Predicted laser-induced temperature rise, according to Eq. (1) vs. radial distance from beam center after 0.01, 01 and 1 sec (numbers next to the curves). Calculations are performed for 5-nm Au NP suspensions in hexane, irradiated with a 405-nm laser beam at 5 mW.

3.4 Time-dependent experiments

Time-dependent data utilizing experimental configuration of Fig. 1(a) were obtained for Ag and Au NP suspensions over a wide range of incident laser power from 405-nm, 633-nm and 785-nm lasers. Most experiments were performed for hexane suspensions, though a few results were obtained in decane and aqueous suspensions. In a typical experiment, an incident laser beam was gated with an AOM in a 3-4 pulse sequence and a time-dependent on-axis detector response in the far field was recorded. Figure 7(a) shows a typical response of a 5-nm Au NP suspension in a hexane solvent, irradiated with a 5-mW 405-nm laser. The transmitted signal decays rapidly once the beam is turned on and remains low for the duration of the trigger. In hexane and decane solvent suspension, the on-axis signal decayed with a similar response on a sub-millisecond scale, Fig. 7(b). By contrast, in a water suspension of 5-nm Ag NPs, no change in the signal was observed under the same irradiation conditions, Fig. 7(b). Since the laser absorption of the two suspensions in Fig. 7(b) is similar, the change in response is attributed to a lower thermo-optic effect in water suspensions and higher thermal conductivity, as opposed to hexane suspensions. No response in either pure hexane or pure water could be observed without nanoparticles under the same irradiation conditions.

Optics EXPRESS

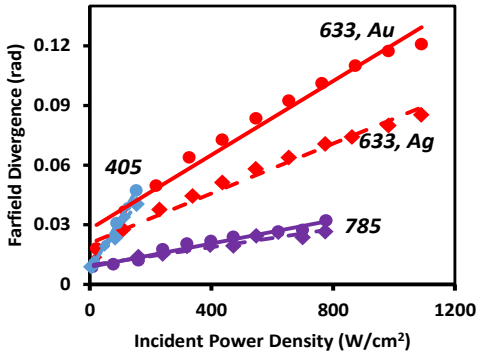

Fig. 6. Far field divergence vs. incident power density for Au and Ag 5-nm NPs in hexane, irradiated at 405-nm, 633-nm and 785-nm wavelengths. Numbers next to the curves indicate incident wavelengths. For the 633-nm irradiation, Au and Ag NP data follow different trends; thus, NP material is indicated as well. The lines are linear regression fits to the data, according to the prediction from Eq. (5).

In order to study potential influence of the boiling point of the solvent material on the intensity-dependent scattering, limited number of irradiations was performed for Ag NPs in decane, a high-boiling point solvent. The results for decane (not shown here) were similar to those observed in hexane. The relevant thermal properties of the two alkanes and water are summarized in Table 3. Clearly, the lack of response in water, compared to the organic solvents, cannot be attributed to the difference in boiling point, but rather to the combination of higher thermal conductivity and lower thermo-optic coefficients of water than either hexane or decane.

Table 3. Thermal Properties of NP Solvents used in the Experiments [16]

Solvent	Boiling Point (°K)	κ (W/m/K)	$D \times 10^7$(m^2/sec)	$-dn/dT \times 10^4$ (/K)
Water	373	0.60	1.43	0.91
n-hexane	341	0.12	0.81	5.20
n-decane	447	0.13	0.82	4.20

The on-axis temporal signal decay became more pronounced with increase in incident laser power. Figure 7(c) and 7(d) present the temporal response of a 5-nm Au NP hexane suspension when irradiated with 405-nm and 633-nm lasers, respectively. Here, the numbers next to the data indicate the incident laser power, while the curves show simulation results with diffraction theory, according to Eqs. (1-3). Good quantitative agreement between the theory and experimental data is observed. The single fitting parameter here is the thermo-optic coefficient, *dn/dT*, of the nanoparticle suspension. The same *dn/dT* coefficient was used for all laser powers shown at a given wavelength for a given suspension. However, different *dn/dT* coefficients were required at 633 nm vs. 405 nm to fit the data. We were thus able to measure dispersion of thermo-optic coefficient for both Au and Ag NP suspensions at 405 and 633 nm, Fig. 8. At 785-nm wavelength, the transient decay was recorded, but no *dn/dT* fitting could be performed because absorption of the suspension was too low to permit unambiguous thermo-optic coefficient extraction.

Optics EXPRESS

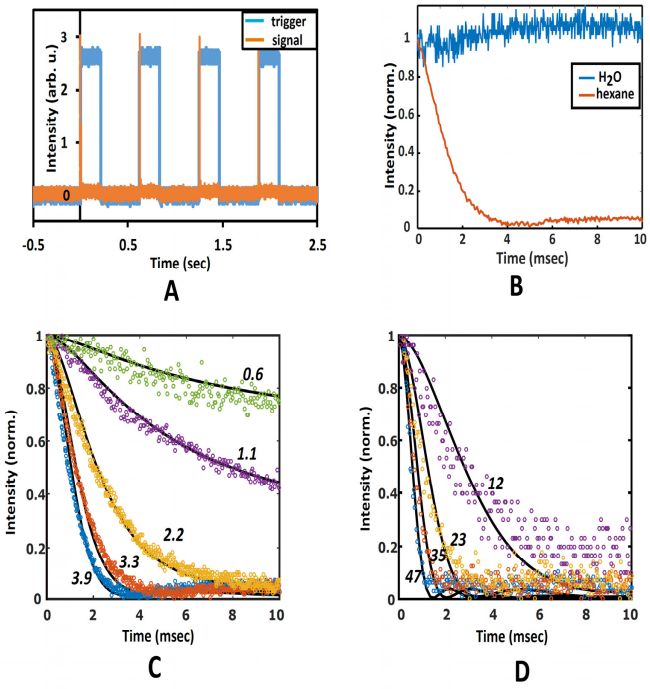

Fig. 7. Time dependent measurements of on-axis laser beam intensity, modulated by an AOM shutter. A. Four cycles of AOM 405-nm 5mW laser modulation ("trigger") and the transmission response ("signal") of the laser through the 5-nm Au NP hexane suspension. B. Transient response of a 405-nm 5 mW laser through a suspension of 5 nm Ag NPs in hexane (orange trace) and H_2O (blue trace). C. 405-nm beam at various incident power (number labels next to curves) incident on a 5-nm Au NP hexane suspension. D 633-nm beam at various incident power (number labels next to curves) incident on a 5-nm Au NP hexane suspension. For both C and D, symbols are experimental data and solid lines are diffraction theory, based on Eqs. (1-3).

Thermo-optic coefficients extracted from numerical fitting for 405-nm and 633-nm incident laser and for both Au and Ag NP suspensions are compared in Fig. 8 with pure hexane and benzene solvents, which have the highest thermo-optic coefficient among common organic solvents [11]. The error bars in extracted data arise from the combination of fitting uncertainty and the experimental error in absorbance coefficient measurements. While dn/dT coefficients at 405 nm for NPs are comparable to that of solvents, the data at 633 nm show a response that is larger by 2x. For transparent solvents, no strong wavelength dispersion would be expected for a thermo-optic coefficient. By contrast, spectral resonances in plasmonic NPs may contribute to the observed dispersion the thermo-optic coefficient for nanosuspensions (see discussion, Section 4).

From time-dependent curves of Fig. 7(c) and 7(d), we extracted the time, T_{50}, over which the initial intensity decays to half of its value, Fig. 9(a), and decay depths in *dB*, Fig. 9(b), as a function of laser power, incident wavelength and NP material. Due to low absorbance of suspension at 785 nm, Fig. 2(a), the response for that wavelength is much weaker. Strongest response is observed for the 633-nm excitation of 5-nm Au NP suspensions, where decay times approaching 200 μsec and attenuation depths of 30 dB are observed. The strong response for this wavelength for Au NPs is a combination of good absorbance and a high thermo-optic coefficient of the suspension, as discussed in the section below.

For 405-nm excitation wavelength, the T_{50} response is similar for both Au and Ag NP systems, which is due to the similar absorption coefficient and thermo-optic coefficient of

Optics EXPRESS

these suspensions. In Fig. 9 (a), the lines connecting the experimental data points are based on an inverse power law fit, which follows approximately from the on-axis attenuation Eq. (4). Extrapolating these data to higher power suggests that sub-100 μs response should be achievable for 405-nm laser power density below 500 W/cm^2.

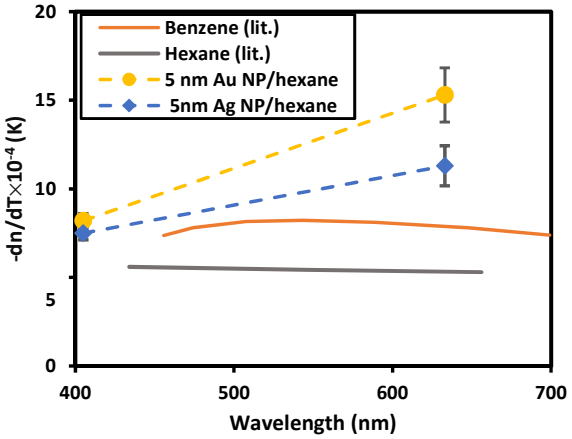

Fig. 8. Comparison of the thermo-optic coefficients from the literature for benzene [11] (solid orange line) and hexane [16] (gray triangles) vs. 5-nm Au (yellow cirles) and Ag (blue diamond) NP suspensions in hexane measured in this study. The dashed lines for the experimental data are drawn to guide the eye.

Beam center attenuation of >30 dB was achieved for 405-nm excitation for both Au and Ag NPs and for 633-nm excitation for Au NPs for power densities below 500 W/cm^2, Fig. 9(b). Below that attenuation point, the Si photodiode was not sensitive enough to detect further decrease in transmitted power. The slope of attenuation for different excitation wavelengths followed similar trends to that of T_{50} – the steepest increase per W/cm^2 was observed at 405-nm excitation, followed by 633-nm Au excitation.

For the single beam experiments, it is not possible to measure intensity recovery when the pump is turned off. In order to address this shortcoming, we performed a limited set of two color pump-and-probe measurements. Here, the probe intensity was kept at a sufficiently low value that resulted in no additional thermo-optic contribution. The recovery times observed in those experiments were on the time scale of <100 milliseconds and were consistent with thermal diffusion. As expected, the recovery times are dependent on the pump duration and power, as well as pump and probe wavelengths.

4. Discussion

The data for thermo-optic coefficient from Fig. 8 suggest a significant effect of NP on the thermo-optic coefficient, especially for the 633-nm wavelength. The effect seems surprising, given a relatively low NP volume concentration of ≤ 1 ppm, but not unprecedented – previous studies have observed an impact of NP suspensions on the thermo-optic coefficient at similarly-low concentrations [8]. Notably, those previous studies reported a low baseline thermo-optic coefficient for their solvent, cyclohexanone; thus, their overall absolute effect was still an order of magnitude below what we measured here.

Considering the effects of particle interactions, the interparticle spacing for all our suspensions is much larger than the particle diameter (Table 2) and no agglomeration could be observed based on absorbance data. Any such possible agglomeration of nanoparticles would result in additional broad spectral shoulders at longer wavelengths [20]. Thus, we rule out the effects of interparticle interactions on observed thermal lensing. Because of the large interparticle separation and small particle diameter, we may also rule out any significant contribution from optical forces [21].

Optics EXPRESS

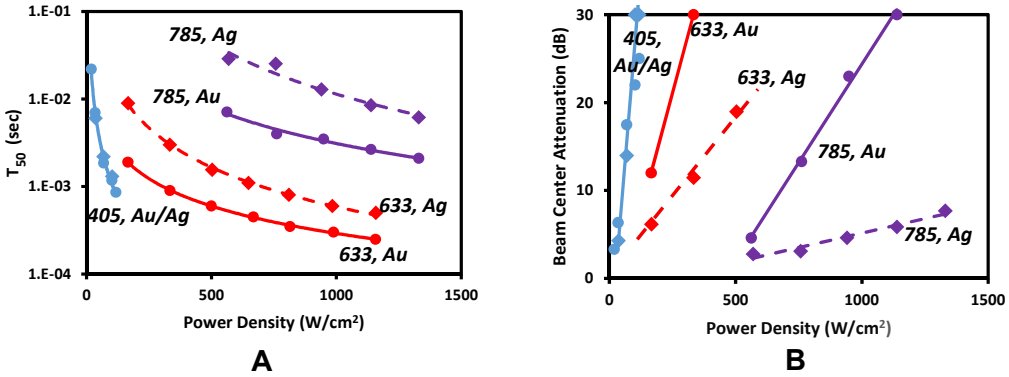

Fig. 9. A. T_{50} on-axis thermal-lensing decay times for Au and Ag NP suspensions for three different wavelengths as a function of incident power density, obtained from experimental decay curves.. The dashed lines are inverse power law fit, as suggested by Eq. (4). B. On-axis attenuation of the laser beam for the same conditions as in A. Lines are drawn to guide the eye. For both figures, labes next to the curves indicate NP material and incident laser wavelength.

Recent work on plasmonic nanosuspensions has demonstrated self-trapping of light and robust soliton propagation, resulting from interplay between optical forces and enhanced polarizability [22]. We do not observe such self-trapping of incident beams under any of our experimental conditions. The plasmonic particle size in our work is an order of magnitude smaller than that in the above reference, and, hence, the polarizability of the particles in our study is one thousand times smaller in the quasistatic limit [23]. Thus, we would not expect the polarizability effects to play a role in our work.

Previous work on Au and Ag nanocomposites in dielectric matrices has shown that the thermo-optic coefficient of the metal-dielectric composite is magnified by surface plasmon resonance (SPR) effect [4, 5]. While quantitative correlation of our studies with that work is complicated because of different host matrices and colloidal concentration, those studies did show strong enhancement of *dn/dT* towards the higher wavelengths as compared to the plasmonic resonance. Such trends are consistent with our observation of increased thermo-optic effect at 633 nm, Fig. 8(a).

Finally, we would like to explore the practical implementation of our strongly observed thermal lensing for beam blocking of high intensity radiation. We consider creating an intermediate focus in a nearly collimated optical system with a pair of lenses. Here, the first lens focuses the incident beam on a cuvette, containing NP suspension. After passing through the cuvette, the beam diverges and is incident on a second apertured lens, placed on the opposite side of focus. For low incident light intensities, Fig. 10(a), the beam is only mildly impacted by cuvette suspension due to low absorbance and the absence of scattering, Fig. 2(a) and 2(b). However, at higher beam intensities, the strong thermal lens effect results in blocking of the beam by the aperture, Fig. 10(b).

The onset of beam blocking occurs at the critical power, P_{cr}, when the thermally induced diffraction exceeds natural beam divergence. Using the variables of Table 1, Eq. (6) and recalling that divergence of a Gaussian beam is $\lambda/\pi\omega$, the equation for critical power is:

$$P_{cr} \sim \frac{1.7\lambda\kappa}{\left|dn/dT\right| f_a} \tag{6}$$

Optics EXPRESS

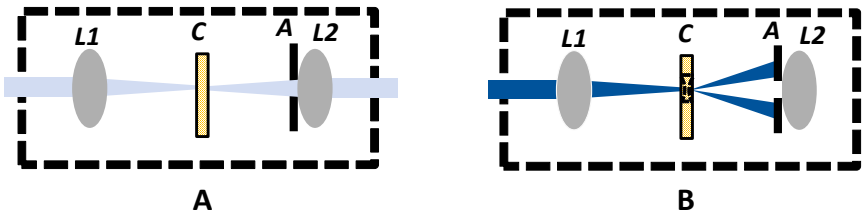

Fig. 10. System implementation of thermo-optic effect for high-power beam rejection. A. a low power beam is brought to an intermediate focus in the cuvette and, then, passes through an aperture and is recollimated by a second lens. B. A high power beam is focused onto a cuvette, but then diverges, due to the thermal lensing effect, and then is blocked by an exit aperture. *L1*, *L2* – lenses. *C* – Cuvette, *A*- apeture.

where f_a is the fraction of light absorbed. According to Eq. (6), focusing of the beam does not improve the amount of beam rejection since the natural beam divergence increases at the same rate to counteract the thermal lens divergence. However, focusing of the beam does reduce the time response of the thermal lens effect, as evident from Eq. (4). Additionally, at higher intensities, other non-linear mechanisms, such as Kerr effect or two-photon absorption may play a role in enhancing optical limiting [24]. Thus, creating an intermediate focus is certainly desirable for fast and efficient beam rejection.

5. Conclusions

We have demonstrated a highly efficient thermal lensing effect in 5-nm of Au and Ag NPs in hexane and decane. On-axis beam decay times as low as 200 μs and power rejection levels of >30 dB were demonstrated at incident laser power densities below 500 W/cm^2 across the visible range. Incident suspension transmission was >70% across the full wavelength range studied. No laser-induced degradation of suspension was found for the highest incident intensities up to 100 W/cm^2.

From the diffraction theory of thermal lensing, we have determined thermo-optic coefficient values across the visible wavelength range. The largest value of $-1.3\text{x}10^{-3}$/K was observed for the 5-nm Au NPs at 633 nm incident wavelength. To our knowledge, this is the highest negative value observed in the literature to date. We believe that this high thermo-optic coefficient results from the synergy between the solvent effect and the plasmonic resonant enhancement of Au NPs.

Finally, we show an implementation of this thermal lensing phenomenon for rejection of high laser intensity through creation of an intermediate focus system. The critical power for the rejection onset depends on the large values of thermo-optic coefficient and the low thermal conductivity of the suspension. At the same time, the speed of the onset is optimized by small beam diameter at focus.

Funding

Department of the Air Force (FA8721-05-C-0002, FA8702-15-D-0001).

Acknowledgment

This material is based upon work supported by the Department of the Air Force under Air Force Contract No. FA8721-05-C-0002 and/or FA8702-15-D-0001. Any opinions, findings, conclusions or recommendations expressed in this material are those of the author(s) and do not necessarily reflect the views of the U.S. Air Force.